nature communications

Article

https://doi.org/10.1038/s41467-025-65453-0

pH calibration allows accurate glucose detection in interstitial fluid via reverse iontophoresis

Received: 13 February 2025

Accepted: 12 October 2025

Published online: 24 November 2025

Check for updates

Wangwang Zhu[1], Haixia Yu[1], Wenjun Li[1], Xi Li[1], Hao Zheng[1], Chengcheng Li[1], Xingguo Zhang[1], Chenxi Jin[1], Mutian Wang[1], Jiaqi Hou[1], Youhao Liu[1], Yuxiao Ma[1], Zhongxu Zhou[1], Miao Deng[1], Peng Guo[1], Mingzhen Li[2], Zhenqiang Song[2], Zhihua Pu[1] ✉ & Dachao Li[1] ✉

Reverse iontophoresis (RI) is a promising non-invasive, wearable technology for the transdermal extraction of interstitial fluid (ISF), which contains rich biomarkers relevant to health status. Despite the advancement of wearable sensors, this technology is still restricted for accurate non-invasive biomarkers detection. The main challenge lies in the instability of ISF extraction during RI. We found that this instability is primarily caused by the skin surface pH variations because of the interaction between the RI-induced H^+ movement and the skin recovery ability. Here, we investigated how the skin surface pH affected RI, theoretically and experimentally; and developed a wearable device and a calibration method to enable accurate non-invasive ISF glucose detection, accordingly. The result showed that glucose prediction accuracy was markedly improved, with mean absolute relative difference (MARD) decreased from 34.44% to 14.78% across both healthy and diabetic volunteers.

With rising living standards and economic progress, personalized diagnostic technologies are gaining increasing attention for their potential in health assessment and early disease diagnosis[1–3]. These technologies typically involve two critical dimensions and trends: wearable, non-invasive monitoring and accurate prediction of physiological status. The breakthroughs of flexible electronics and nanotechnology in recent years may address the requirements for wearables[4,5], however, it is still a big challenge to achieve accurate and non-invasive prediction[6]. Biomarkers, such as metabolites[7–9], hormones[10,11], electrolytes[12], and proteins[13,14], serve as pivotal roles in achieving accurate prediction of physiological status[6,15,16]. These biomarkers, derived from biofluids such as sweat[17–20], tears[21], saliva[22], urine[23], and interstitial fluid (ISF)[24–27], have already been explored for wearable and non-invasive health monitoring. Notably, among these biofluids, ISF contains the most categories of biomarkers, and its composition is closely correlated with blood-derived information[28,29]. Therefore, we think that ISF may be the best choice to achieve accurate and non-invasive biomarker detection.

Non-invasive ISF detection is currently achievable through radiofrequency[30], ultrasound[31], optics[32], metabolic heat conformation[33], and reverse iontophoresis (RI)[34–37]. The former four methods face challenges for accuracy due to indirect measurement and interferences from complex tissue, especially from omnipresent blood[38]. In contrast, RI provides direct extraction and detection of ISF, holding great potential for accurate analysis of biomarkers[24]. RI, first introduced by Richard H. Guy's group in 1989, has undergone significant advancements over the years[39]. In 2001, *Cygnus Inc*. launched the GlucoWatch® Biographer, the first and only commercial device based on RI, demonstrating the potential for wearable and non-invasive glucose detection[40]. Unfortunately, the device was discontinued in 2007 due to several limitations, including skin irritation, sweat-induced interference, discomfort of wearing, measurement

[1]State Key Laboratory of Precision Measurement Technology and Instruments, Tianjin University, Tianjin, China. [2]NHC Key Lab of Hormones and Development and Tianjin Key Lab of Metabolic Diseases, Tianjin Medical University Chu Hsien-I Memorial Hospital & Institute of Endocrinology, Tianjin, China.
✉e-mail: puzhihua@tju.edu.cn; dchli@tju.edu.cn

inaccuracies from sensor-skin displacement by rigid components, and instability of ISF extraction[41]. Recent advancements in flexible electronics and nanotechnology have addressed many of these challenges, such as skin irritation[42], sweat-induced interference[38], and discomfort of wearing[5,43–45], reigniting interest in RI for wearable and non-invasive biomarkers detection[46–49]. Despite these innovations, the issue with accurate detection remains. We found that the key issue lies in the fluctuations of ISF extraction[34].

Under the influence of the skin's physiological negative charge, RI facilitates the transdermal extraction of ISF by applying a mild current to the skin[50]. This process is driven primarily by the electromigration of cations in the electrical double layer (EDL), thereby making the electroosmotic flow of small neutral biomarkers, for example, glucose[51]. Here, we found that the EDL at the interface between the skin and the RI electrodes significantly affects this electroosmotic flow. Specifically, the extracted H^+, along with the release of additional H^+ from biochemical reactions, collectively leads to changes in the pH of the RI-induced fluid accumulated at the skin surface and within the epidermal electroosmotic microchannel (referred to as the skin surface pH in this study). The skin recovery mechanisms, including natural barriers such as sweat glands and the stratum corneum that maintain homeostasis and prevent excessive polarization[52–54], will hinder the change. The interaction leads to the fluctuations of skin surface pH, which changes the zeta potential (ZP) of the EDL[55,56], thereby causing instability in the electroosmotic flow of ISF accordingly.

To validate this hypothesis, here we provide a detailed theoretical analysis of how skin surface pH influences ISF extraction by modulating the ZP of keratin, thereby directly affecting ISF extraction and subsequent detection accuracy. We conducted a numerical simulation to elucidate these effects; we designed and fabricated an epidermal electronic device integrating symmetric ISF extraction electrodes, glucose, Na^+, and pH sensors for experimental investigation. Theoretical experiments were conducted firstly to validate our hypothesis. Then, a skin surface pH calibration method was developed and validated to enable accurate and non-invasive ISF glucose detection through in-vitro and in-vivo experiments.

Results

Theoretical analysis of effect of skin surface pH on RI

Theoretical analysis. Human skin is composed of dermis, epidermis, stratum corneum (SC), and hydrolipid film (HF) that overlays the SC (Fig. 1a). At the interface between the HF and the SC, charge separation occurs due to the interaction of solid and liquid phases. This phenomenon leads to a spatial distribution of potential differences near

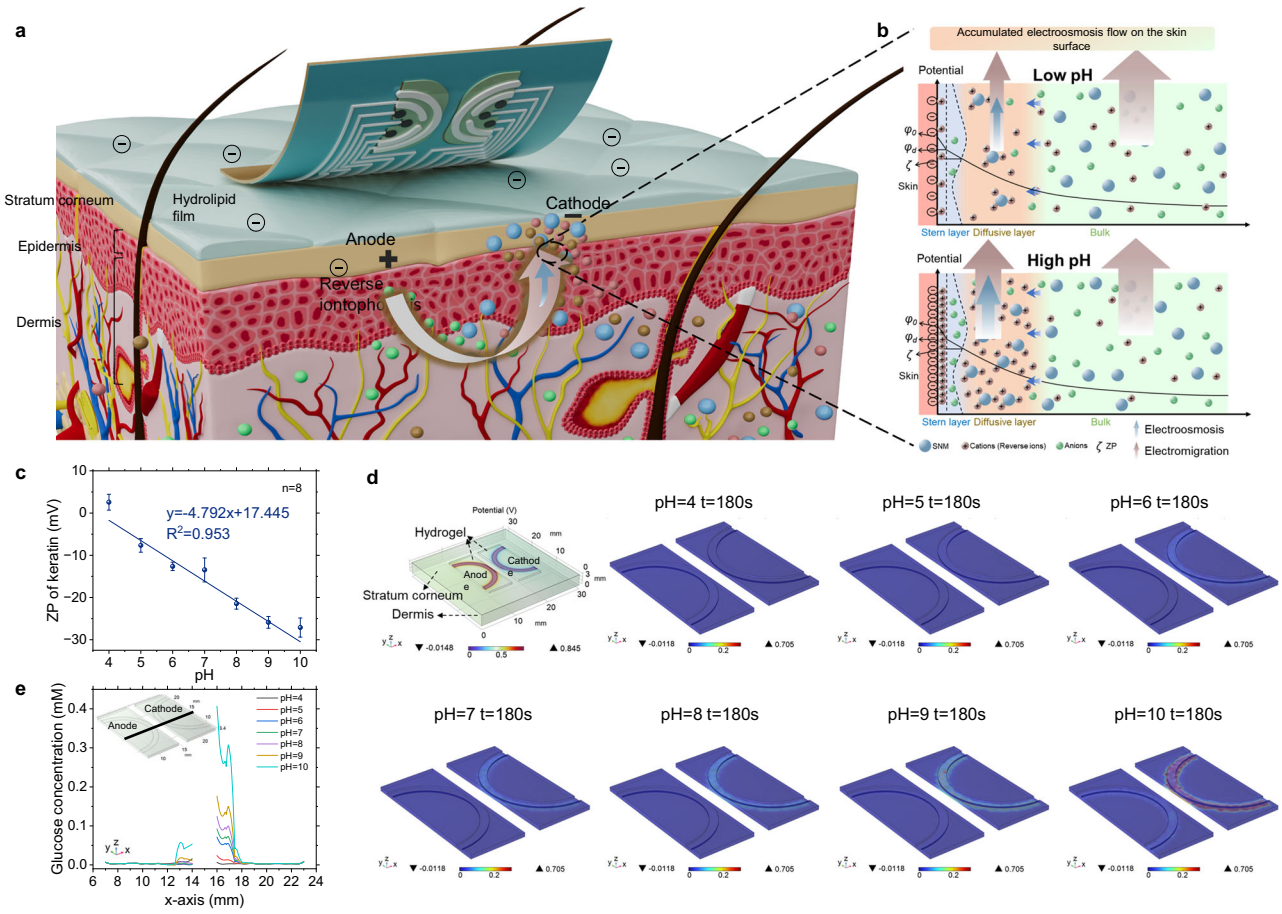

Fig. 1 | Schematic of the skin surface pH-influenced ISF extraction based on RI for accurate and non-invasive biomarkers analysis. a Schematic of the skin structure and ISF extraction process by RI. The negatively charged, porous nature of human skin enables the migration of counterions, such as Na^+ and H^+, towards the cathode under an applied voltage, generating an electroosmotic flow of neutral molecules such as glucose. **b** The EDL structure of the skin and the electroosmosis under low and high pH conditions, with the ZP at the shear plane. SNM, small neutral molecules; ZP, zeta potential. **c** ZP measurements of keratin at different pH levels. Data are presented as mean values ± SD ($n = 8$ technical replicates). **d** Numerical simulation of the distribution of extracted glucose concentrations under different pH conditions using COMSOL, with an applied current of 150 μA cm^{-2} for 3 min. Top-left: Simulation model of the skin, hydrogel, and electrodes for ISF extraction, along with the potential distribution after applying a constant current. **e** Glucose concentration distributions within the hydrogel, derived from a cross-sectional line extending from the anode to the cathode hydrogel, with coordinates ranging from (7, 15, 3.07) to (23, 15, 3.07) (indicated by the black line in the inset).

the interface, thereby establishing the EDL structure, which comprises a Stern layer and a diffusion layer. RI extraction of ISF hinges on two key mechanisms: the electromigration of ions and the electroosmosis of small neutral molecules. The electromigration involves ionic fluxes originating from both the bulk ISF and the diffusion layer. In contrast, the driving force for the electroosmotic transport of small neutral molecules primarily arises from the migration of counterions (carrying charges opposite to the skin surface) within the diffuse layer under an applied electric field. Consequently, the concentration of these counterions governs the electroosmotic velocity (Fig. 1b, Supplementary Note 1).

The skin's inherent negative charge under physiological conditions results in cation-dominated ion flux (counterions) within the EDL during RI. This cation flux facilitates the movement of small neutral molecules, e.g., glucose, towards the cathode. In this process, Na^+ dominates the ion flux and acts as the primary carrier in the EDL, while extracted H^+ and released H^+ from biochemical reactions at the epidermal interface alter the skin surface pH. Additionally, the skin recovery mechanisms, including natural barriers such as sweat glands and the stratum corneum, help maintain homeostasis and prevent excessive polarization[52–54], thereby mitigating the pH changes induced by RI. The interaction between the H^+ movement and the skin recovery ability makes the fluctuations of skin surface pH. Fluctuations in skin surface pH indeed modulate the charge density of the skin, affecting the quantity of counterions (mainly Na^+) in the EDL diffusion layer, which in turn leads to the fluctuations of electroosmosis.

The charge density of the skin can be reflected by the ZP (the potential at the slip plane)[55]. Particularly, the negative charge of skin originates from the acidic nature of the HF, which is induced by the sweat secretion, sebum degradation, and microbial metabolites[57,58]. The ionization state of carboxylic groups within the keratin of SC varies with pH, exhibiting a neutral state at the isoelectric point (pI) where the pH ranges from 4 to 4.5, a positive charge state below the pI while a negative charge state exceeds the pI[59,60] (Supplementary Fig. 1a). We preliminarily explored the influence of skin surface pH on ZP using keratin (main components of SC), and the results revealed the great influence and a negative correlation between ZP and pH (Fig. 1c, Supplementary Table 1).

Numerical simulation. Here, we use glucose as an example to investigate the impact of pH variations on electroosmotic flow, an ISF extraction model was developed in COMSOL, incorporating ZP measurements across different pH levels (Fig. 1c, Supplementary Note 2 and Supplementary Table 1). Simulation results revealed that at pH 4, the glucose concentration at the anode is higher than at the cathode. Conversely, when the pH exceeds 4, the glucose concentration at the cathode becomes significantly higher than that at the anode, and both electrodes exhibit a rise in glucose concentration as pH increased, aligning with the ZP-dependent extract mechanism by RI (Fig. 1d, e, Supplementary Fig. 1b–h).

Design and characterization of the epidermal electronic device

Design and fabrication of the wearable device. To validate our hypothesis and theoretical analysis, we designed a wearable electronic device accordingly, which incorporated a pair of RI extraction electrodes for ISF extraction, glucose sensors, Na^+ sensors and pH sensors for fluxes measurement and skin surface pH monitoring. Specifically, the device is divided into two symmetrical sensing regions, Part A and Part B. Each part comprises a semi-circular RI electrode, a glucose sensor, a Na^+ sensor, and a pH sensor (Fig. 2b). The layer assembly of the device consists of a flexible polyimide (PI) substrate layer, enabling seamless conformity to skin deformations for comfortable wearing; an Ag conductor layer to ensure stable electrical connections; a sensors layer for simultaneous ISF extraction, glucose, Na^+, and pH detection; a patterned 3 M adhesive layer for attachment to the skin and precise hydrogel patterning; and a hydrogel layer serving as the ISF collection reservoir and microreaction chamber (Fig. 2c, d). The epidermal device was fabricated by screen printing, followed by layer-by-layer surface functionalization (Supplementary Fig. 4).

Characterization of the wearable device. We firstly conducted comprehensive characterizations of the proposed device to validate its functionality. Scanning Electron Microscopy (SEM) and X-ray Photoelectron Spectroscopy (XPS) of the electrodes confirm the successful fabrication and functionalization of the device (Supplementary Figs. 6, 7). The detection principle of this device involves two electrochemical mechanisms: an enzyme-catalyzed reaction that converts glucose concentration into amperometric current (i-t) under the applied bias voltage; and a Nernstian response that converts Na^+ concentration and pH into potentiometric voltage (Fig. 2a).

H_2O_2, an intermediate product of glucose oxidation, was initially measured to evaluate the performance of the electrodes, which exhibited excellent performance with a sensitivity of 0.44 μA mM^{-1} (Supplementary Fig. 8). Then, a series of comprehensive tests were conducted on the glucose sensor, including stepwise, sensitivity, consistency, selectivity, and storage stability. Stepwise testing revealed that the steady-state current of the i-t response increased with glucose concentration (Fig. 2e). The glucose sensor exhibited a highly linear response, with a sensitivity of 236.42 nA mM^{-1} from 0–3 mM (Fig. 2f) and 28.22 nA mM^{-1} from 3 to 30 mM (Supplementary Fig. 9d). Sensor-to-sensor consistency was well maintained with minimal variation in sensitivity across three devices (Supplementary Fig. 9h). The sensor also demonstrated high selectivity against a range of potential interfering species (Fig. 2g, Supplementary Fig. 9e–g). After 14 days of storage, the sensor retained ~75% of its original sensitivity (Fig. 2h, Supplementary Fig. 9i). Considering that the fluctuations in skin surface pH during RI process affect the performance of the glucose sensor, sensitivity testing was performed under different pH conditions (Fig. 2i, Supplementary Fig. 10e). The relationship between the sensitivity and pH presented as a quadratic curve. At the pH of 7, normal pH of ISF, the sensitivity reached 298.56 nA mM^{-1} (Fig. 2j). The ultraviolet (UV) absorbance (ABS) of H_2O_2 generated by glucose oxidase (GOx) at varying pH values exhibited a comparable trend in sensitivity (Supplementary Fig. 10a–d), revealing that pH impacts the performance of glucose sensor through diminishing the activity of GOx. Consequently, prior to calculating the glucose concentration through sensitivity, a pH correction for sensitivity is required first, which is essential for accurate glucose detection. The test results for different pH values and glucose concentrations demonstrated that higher glucose detection accuracy was attained after pH correction (Fig. 2k, l, Supplementary Fig. 11). Similar to the glucose sensor, the Na^+ sensor exhibited robust performance across the testing of step-response (Fig. 2m), sensitivity (52 mV $decade^{-1}$) (Fig. 2n), stability (Supplementary Fig. 12a), consistency (Supplementary Fig. 12d), selectivity (Fig. 2o, Supplementary Fig. 12c), and storage life (Fig. 2p, Supplementary Fig. 12e). The pH sensor demonstrated excellent outcomes in multiple evaluations: step-response (Fig. 2q, Supplementary Fig. 13c), sensitivity (−52 mV $decade^{-1}$) (Fig. 2r, Supplementary Fig. 13a), stability (Supplementary Fig. 13b), consistency (Supplementary Fig. 13e), selectivity (Fig. 2s, Supplementary Fig. 13d), and storage life (Fig. 2t, Supplementary Fig. 13f). Utilizing an environment-controlled flexible electronic system (FE-SDT), the device maintained functionality during mechanical deformation, thus making it ideal for wearable applications (Supplementary Figs. 14, 15). These results confirm the robust performance of the proposed wearable device.

Experimental validation of effect of skin surface pH on RI

Na^+ flux under different skin surface pH. To further corroborate the hypothesis regarding the influence of skin surface pH on RI, validation experiments were carried out employing a Franz diffusion cell system

https://doi.org/10.1038/s41467-025-65453-0

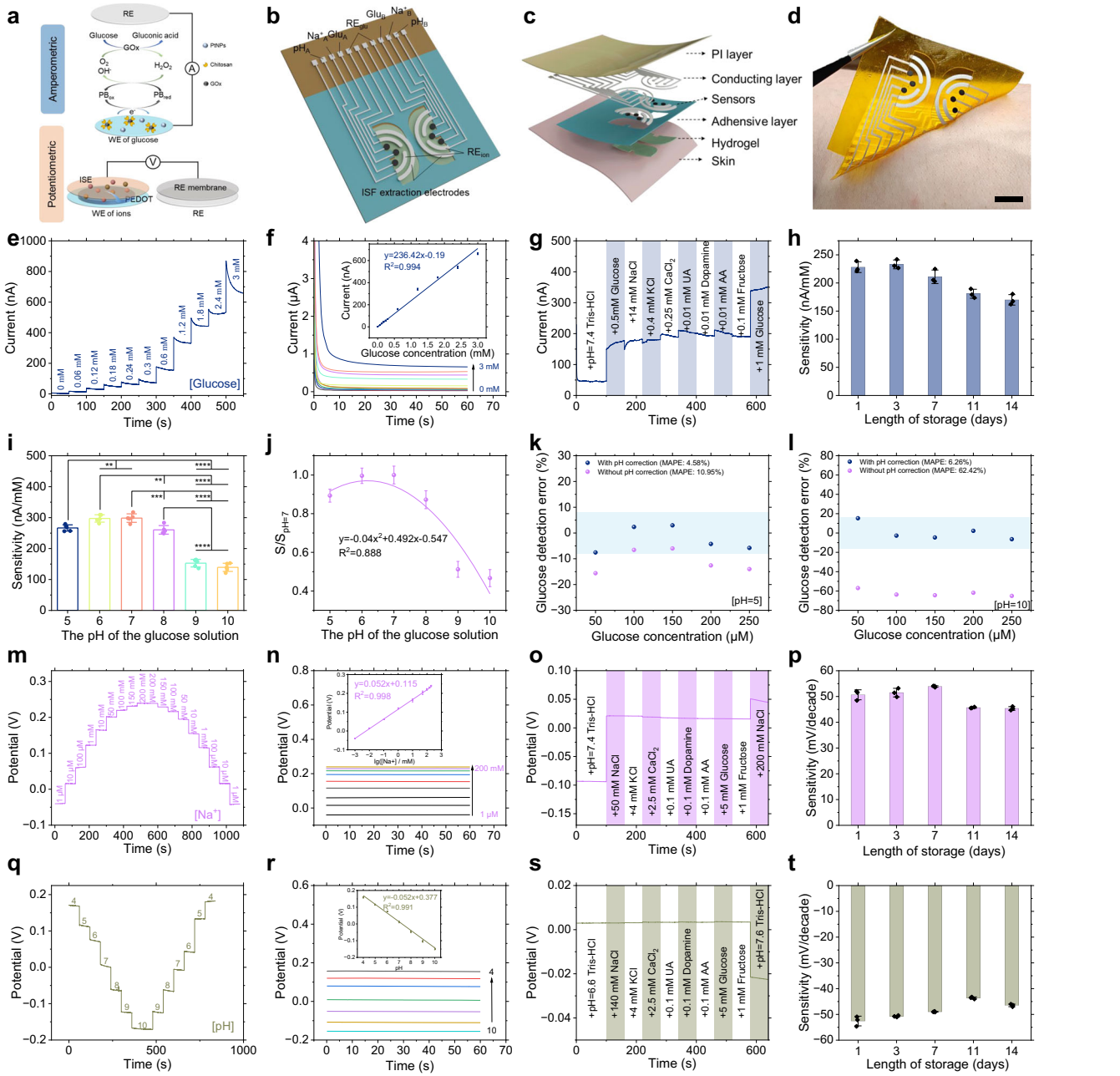

Fig. 2 | Design and characterization of the wearable device. a Schematic illustrating the mechanism of glucose measurement by CA and Na^+/pH detection by OCP. CA, chronoamperometry; OCP, open-circuit potential. **b**, **c** Layer assembly (**b**) and schematic design (**c**) of the wearable device. **d** Optical images of the fabricated device on the forearm skin. Scale bars, 1 cm. **e**, **f** Stepwise testing of the glucose sensor from (**e**), and i-t curves with the corresponding correlation curve (inset) from 0 to 3 mM at an initial potential of −0.1 V versus RE (**f**) ($n = 3$ technical replicates). **g** Selectivity performance of the glucose sensor at low concentrations. **h** Storage stability of the glucose sensor over 14 days ($n = 3$ independent sensors). **i** Sensitivity of the glucose sensor under varying pH conditions, performed in Tris-HCl buffer solutions with pH values of 5, 6, 7, 8, 9, and 10 ($n = 5$ technical replicates). pH 5: $P = 0.0087$ (vs. pH 6), $P = 0.0061$ (vs. pH 7), $P < 0.0001$ (vs. pH 9 or 10); pH 6: $P = 0.0013$ (vs. pH 8), $P < 0.0001$ (vs. pH 9 or 10); pH 7: $P = 0.0009$ (vs. pH 8), $P < 0.0001$ (vs. pH 9 or 10); pH 8: $P < 0.0001$ (vs. pH 9 or 10). Statistical analysis was performed using one-way ANOVA with Tukey's multiple comparison. $^{**}P < 0.01$, $^{***}P < 0.001$, and $^{****}P < 0.0001$. **j** Calibration curve of glucose sensitivity as a function of pH. Glucose sensitivity was normalized at pH 7, revealing a quadratic relationship between glucose sensitivity and pH ($n = 5$ technical replicates). S, sensitivity. **k**, **l** Glucose detection error with and without pH correction at pH 5 (**k**) and 10 (**l**). **m**, **q** Reversibility of the Na^+ sensor (**m**) and pH sensor (**q**). **n**, **r** Potentiometric responses and corresponding correlation curve (inset) of the Na^+ sensor (**n**) and pH sensor (**r**) ($n = 3$ technical replicates). **o**, **s** Selectivity of the Na^+ sensor (**o**) and pH sensor (**s**) under various interferences. **p**, **t** Storage stability of the Na^+ sensor (**p**) and pH sensor (**t**) over 14 days ($n = 3$ independent sensors). Data are presented as mean values ± SD.

in conjunction with a Strat-M® membrane to simulate the ISF extraction process (Fig. 3a, Supplementary Fig. 16). Tris-HCl buffer solutions at varying pH levels were added into the receiver chamber to simulate different skin surface pH environments, while NaCl solutions containing glucose were placed in the donor chamber to simulate ISF. Since the extraction process of RI involves the Na^+ flux by electromigration and the glucose flux by electroosmosis, and the primary counterions in a physiological state are Na^+, the impact of skin surface pH on the Na^+ flux was explored firstly. The significant difference in potential response of the Na^+ sensor in the receiver chamber before

https://doi.org/10.1038/s41467-025-65453-0

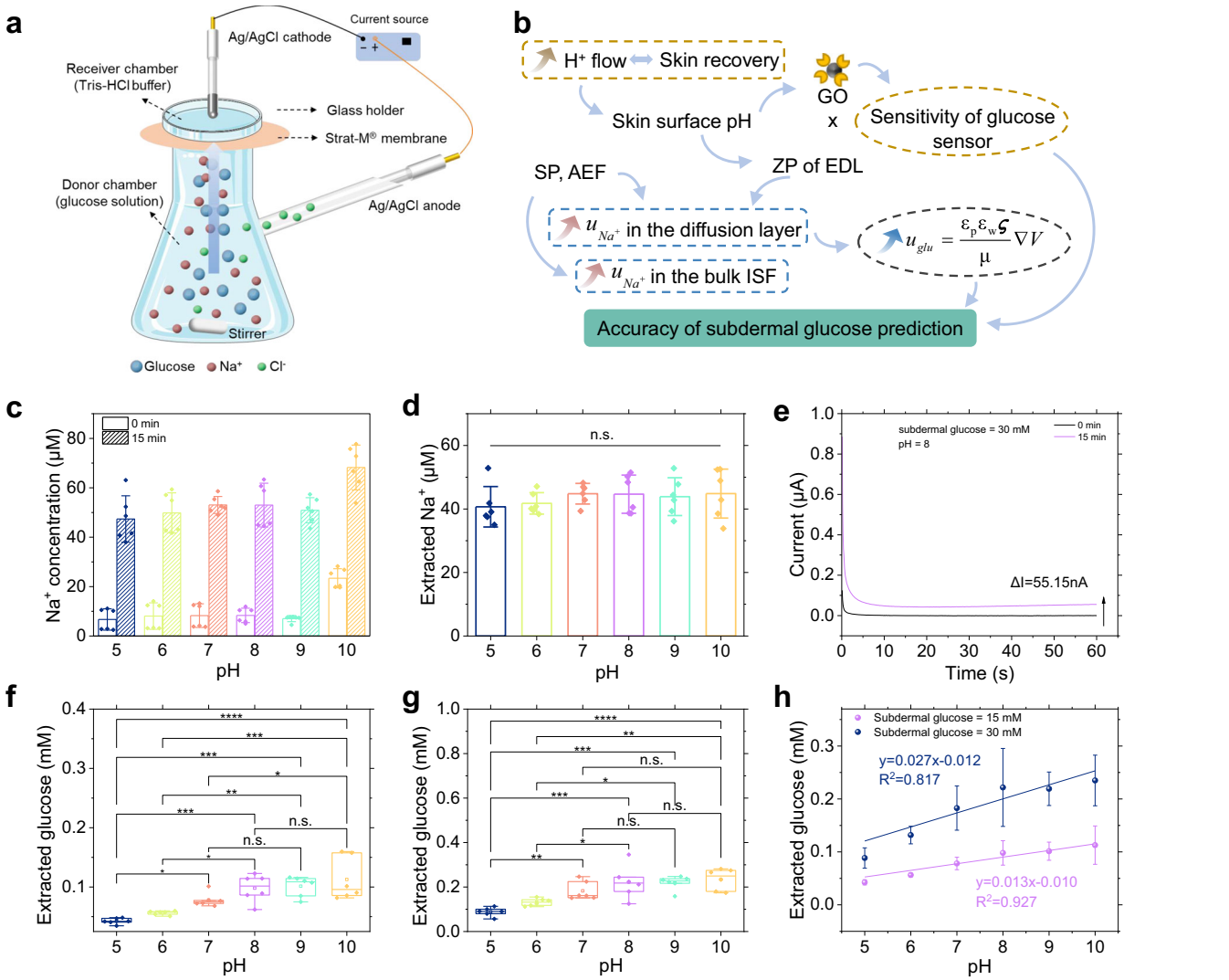

Fig. 3 | Experimental validation of the effect of skin surface pH on RI. **a** Schematic of the simulated ISF extraction system using a Franz diffusion cell, applying a 0.5 mA current for 15 min, extraction of RI. The donor chamber contains 15 mL of glucose solution with 140 mM NaCl, while the receiver chamber holds 3 mL of Tris-HCl buffer solution at varying pH levels. **b** The mechanism by which Na^+ flux and skin surface pH affect the accuracy of subdermal glucose prediction based on RI. SP, skin property; AEF, applied electrical field. **c**, **d** Na^+ concentrations before and after 15 min of RI extraction at varying pH levels (**c**) and extracted Na^+ concentration at varying pH levels (**d**). Data are presented as mean values ± SD ($n = 6$ technical replicates). **e** I-t responses at pH 8 for 30 mM subdermal glucose before and after 15 min of RI extraction. **f**, **g** Extracted glucose concentrations under varying skin surface pH values (simulated by Tris-HCl buffer) with subdermal glucose concentrations of 15 mM (**f**) and 30 mM (**g**). The box spans the 25th–75th percentiles, the horizontal line marks the median, and the whiskers extend to the minimum and maximum non-outlier values. ($n = 6$ technical replicates). In (**f**), pH 5: $P = 0.0394$ (vs. pH 7), $P = 0.0004$ (vs. pH 8), $P = 0.0002$ (vs. pH 9), $P < 0.0001$ (vs. pH 10); pH 6: $P = 0.0104$ (vs. pH 8), $P = 0.005$ (vs. pH 9), $P = 0.0003$ (vs. pH 10); pH 7: $P = 0.0481$ (vs. pH 10). In (g), pH 5: $P = 0.0079$ (vs. pH 7), $P = 0.0001$ (vs. pH 8), $P = 0.0001$ (vs. pH 9), $P < 0.0001$ (vs. pH 10); pH 6: $P = 0.0125$ (vs. pH 8), $P = 0.0161$ (vs. pH 9), $P = 0.0032$ (vs. pH 10). **h** Correlation curves of extracted glucose concentrations and skin surface pH. Data are presented as mean values ± SD ($n = 6$ technical replicates). Statistical analysis was performed using one-way ANOVA with Tukey's multiple comparison. *$P < 0.05$, **$P < 0.01$, ***$P < 0.001$, and ****$P < 0.0001$; n.s., non-significant.

and after 15 min of RI extraction clearly confirmed the effective Na^+ extraction (Fig. 3c). Notably, the extracted Na^+ flux exhibited minimal variation across different pH levels, confirming that changes in skin surface pH has a negligible impact on the Na^+ flux (Fig. 3d, Supplementary Table 3). The reason may be that the electromigration of Na^+ predominantly occurs in the bulk solution, while the pH value only affects the Na^+ flux in the diffusion layer of the EDL.

Glucose flux under different skin surface pH. Experiments were also conducted to explore the impact of skin surface pH on the electroosmotic extraction of glucose. The i-t responses of the glucose sensor before and after extraction showed a substantial increase in the steady-state current, underscoring the effective glucose extraction (Fig. 3e, Supplementary Figs. 17–22, and Supplementary Table 4). After converting this current difference into the extracted glucose flux, it was discovered that the extracted glucose flux rose progressively as the increasement of skin surface pH. Moreover, higher glucose levels in the subcutaneous ISF at 30 mM (Fig. 3g, Supplementary Fig. 23b) led to greater extracted glucose flux compared to the 15 mM one (Fig. 3f, Supplementary Fig. 23a). The linear regression analysis across the entire pH range 5–10 showed a slope significantly different from zero ($p = 0.00207$ at 15 mM and $p = 0.01343$ at 30 mM) and a high determination coefficient ($R^2 = 0.927$ at 15 mM and $R^2 = 0.817$ at 30 mM), indicating a clear overall upward trend in extracted glucose with increasing pH. And the results demonstrated that, in

the cases of subcutaneous glucose levels at 15 mM and 30 mM, the extracted glucose concentration was increased by 0.013 mM and 0.027 mM per each 1 pH unit increment, respectively (Fig. 3h). Interestingly, the increase ratios are both ~33%/pH, confirming the uncorrelation between the electroosmotic velocity and the subdermal glucose concentrations. These results verify that skin surface pH affects the electroosmotic flow of glucose significantly, requiring a calibration model to achieve accurate glucose prediction.

Skin surface pH calibration for subdermal glucose prediction

The skin surface pH calibration method presented in this work tackles two crucial aspects: the correction of glucose sensor sensitivity and the calibration of glucose extraction flux (Fig. 3b). The former rectifies the change in enzyme activity resulting from pH variations, which directly influence the performance of the glucose sensor. The sensitivity of the glucose sensor exhibits a quadratic relationship with pH as described by equation (1.10). The latter centers on mitigating the deviations in glucose extraction flux linearly induced by skin surface pH changes. In this RI process, Na^+ flux induces glucose flux; therefore, it serves as the base of subdermal glucose prediction, and it also indicates the different skin properties of different person[38,61]. The comprehensive calibration and subdermal glucose prediction equation is presented as equation (1.25), with detailed derivations in the Supplementary Note 3.

In-vitro evaluation of the calibration method and wearable device

Dynamic changes in glucose and skin surface pH during RI extraction. Capitalizing on the established linear relationship between skin surface pH and glucose extraction flux, we performed in-vitro experiments to appraise the precision of glucose prediction both with and without pH calibration (Fig. 4a, Supplementary Fig. 24). Artificial skin was used in the in-vitro experiments, it was assumed that the physical properties of the skin remained constant during the RI process, thus the Na^+ flux would be a constant at a certain extraction condition. Therefore, the Na^+ flux was not tested here. To minimize errors from repeated ISF extractions, glucose and pH measurements from five consecutive cycles were used for validation. The subcutaneous simulated ISF was a solution containing 140 mM NaCl with glucose concentrations of 6, 12, 18, 24, and 30 mM, respectively. The in-vitro testing findings of this device were categorized into three segments: Part A, Part B, and the overall test results. When the subcutaneous glucose concentration was 12 mM, the steady-state current of the i-t responses acquired from Part A and Part B increased significantly over the five consecutive RI extractions (Fig. 4b, e, Supplementary Figs. 30, 31). Simultaneously, the skin surface pH detected by the pH sensors in both parts exhibited significant fluctuations (Fig. 4c, f, Supplementary Figs. 30, 31). The extracted glucose concentrations were linearly fitted against the extraction times of RI. Herein, the slope (denoted as Slope 1) derived from the regression represents the extracted glucose by a single instance of RI. Notably, after applying pH calibration, the slope 1 for Part A and Part B exhibited a marked increase, with the Slope 1 for Part A augmenting by 8.1% (Fig. 4d) and that for Part B growing by 7.5% (Fig. 4g). The different increase between the Part A and Part B may be caused by the different changes of electrical property at the interface of artificial skin and electrodes. The increase reflects the suppressive effect of declining skin surface pH on glucose flux during consecutive RI cycles, which is essential for subsequent prediction of subcutaneous glucose concentrations. The extraction results at subdermal glucose concentrations of 6 mM (Supplementary Figs. 28, 29), 18 mM (Supplementary Figs. 32, 33), 24 mM (Supplementary Figs. 34, 35), and 30 mM (Supplementary Figs. 36, 37) were also recorded and analyzed (Supplementary Table 4).

Relationship between extracted and subcutaneous glucose concentrations. A linear fit of the extracted glucose (represented by the fitted slope 1) against the subdermal glucose concentrations revealed a consistent positive linear correlation (denoted as slope 2) for both Part A and Part B of the device (Supplementary Fig. 38). The Slope 2 serves as the foundation for subsequent subcutaneous glucose prediction in the experiments. The results showed that following pH calibration, the Slope 2 exhibited an increment, with an increase of 12.1% in Part A and 6.2% in Part B of the device (Supplementary Fig. 38). To achieve higher-frequency measurements, which are of great importance for practical wearable applications, the measurements from Part A and Part B are combined to obtain the overall results (Supplementary Fig. 27). The results further confirmed the linear relationship with 9.9% increase of slop after pH calibration (Fig. 4h), underlining the impact of pH calibration on subsequent glucose prediction.

Subcutaneous glucose prediction using the calibration method and wearable device. After obtaining the relationships of extracted glucose to simulated subcutaneous glucose with and without pH calibration, we performed RI extraction and detection on additional solutions with pre-determined subcutaneous glucose concentrations. Specifically, solutions with subcutaneous glucose concentrations of 5 mM, 8 mM, 12 mM, 18 mM, and 25 mM were individually subjected to our experimental procedures. The results demonstrated a substantial elevation in glucose prediction accuracy after pH calibration, with the mean absolute percentage error (MAPE) decreased markedly from 11.2% to 2.9% (Fig. 4i). This improvement highlights the efficacy of skin surface pH calibration in reducing the inaccuracies caused by pH fluctuations during RI. These experiments serve as a preliminary validation of the proposed skin surface pH calibration method and device.

In-vivo evaluation of the calibration method and wearable device

To further validate the applicability of the wearable device and the pH calibration method in practice, oral glucose tolerance tests (OGTT) were performed on 6 healthy participants and 15 Type II diabetic patients (Fig. 5a). During the 2.5-h experiment, fluctuations were observed in the extracted glucose flux, skin surface pH, and Na^+ flux. The slight fluctuations in Na^+ extraction are likely attributable to changes in skin permeability induced by prolonged RI extraction[38]. These three curves showed abrupt changes between consecutive data points throughout the test, which were attributed to the alternating polarity of ISF extraction (Fig. 5b, c left, Supplementary Fig. 39). Glucose prediction accuracy was evaluated under various calibration conditions: without calibration, with Na^+ calibration only, and with cooperative Na^+ and pH calibration (Fig. 5b, c right, Supplementary Fig. 39). The results showed that after cooperative calibration, the glucose prediction curve closely aligned with the reference curve. Clarke's error grid analysis of healthy participants demonstrated a progressive increase in the percentage of data points falling within zone A: from 56.67% without calibration to 58.34% with Na^+ calibration (61.54% reported by Pu et. al.[38]), and 78.33% with cooperative Na^+ and pH calibration (Fig. 5d, g, Supplementary Table 6). The results of diabetic patients showed that the percentage of data points falling within zone A and B: from 70% without calibration to 90% with cooperative Na^+ and pH calibration (Fig. 5h, k, Supplementary Table 6). Mean absolute relative difference (MARD) of healthy individuals further corroborated this trend, significantly decreasing from 25.49% (without calibration) to 20.04% (Na^+ calibration) and 10.91% (cooperative calibration) (MARD ≤ 20% by FDA)

https://doi.org/10.1038/s41467-025-65453-0

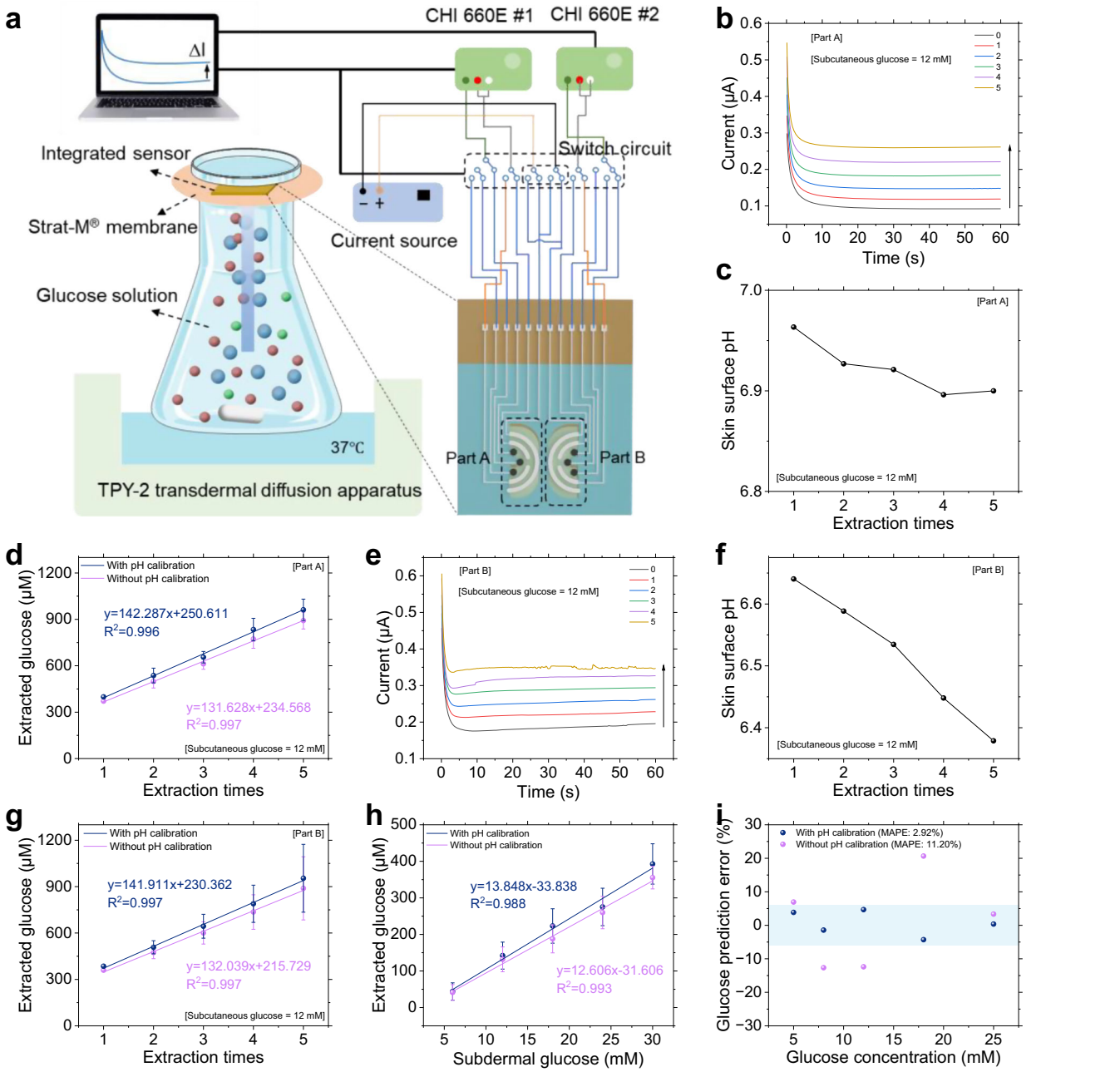

Fig. 4 | In-vitro evaluation of the calibration method and wearable device. **a** Schematic of the in-vitro ISF extraction and testing system. The system consists of a TPY-2 transdermal diffusion apparatus to simulate ISF flow and maintain temperature at 37 °C, a source providing a current of 150 μA cm^{-2} for 3 min for one extraction cycle, electrochemical workstations (CHI 660E) for glucose, Na^+, and pH detection, a switching circuit for automatic control of ISF extraction (alternating current polarity during successive extractions) and measurements, and a Franz diffusion cell to replicate the ISF extraction process. **b**, **e** I-t responses of Part A (**b**) and Part B (**e**) of the device under 12 mM subcutaneous glucose, with five successive extractions of RI. **c**, **f** Skin surface pH variations of Part A (**c**) and Part B (**f**) of the device under 12 mM subcutaneous glucose, with five successive extractions. **d**, **g** Correlation curves of extracted glucose and extraction times for Part A (**d**) and Part B (**g**) of the device under 12 mM subcutaneous glucose, with and without pH calibration ($n = 5$ technical replicates). **h** Correlation curves of extracted glucose and subcutaneous glucose with and without pH calibration of the overall test results (ten data points per subdermal concentration obtained from Parts A and B). **i** Glucose prediction error of the device with and without pH calibration at subcutaneous glucose concentrations of 5, 8, 12, 18, and 25 mM. MAPE, mean absolute percentage error. Data in (**d**, **g**, **h**) are presented as mean values ± SD.

(Fig. 5g). The results of diabetic patients showed that MARD was changed from 42.11% (without calibration) to 33.24% (Na^+ calibration) and 18.10% (cooperative calibration) (Fig. 5k). Following cooperative calibration, the MARD observed across all volunteers was 14.78% (Supplementary Fig. 41). These results indicate that skin surface pH calibration plays a vital role in accurate predication of subdermal glucose based on RI, especially for prolonged extraction. The results also highlight the potential of the developed device and the proposed pH calibration method as a wearable and non-invasive tool for continuous biomarkers monitoring.

Discussion

This work reveals that skin surface pH significantly fluctuates during prolonged RI, which exerts a critical influence on the performance of

https://doi.org/10.1038/s41467-025-65453-0

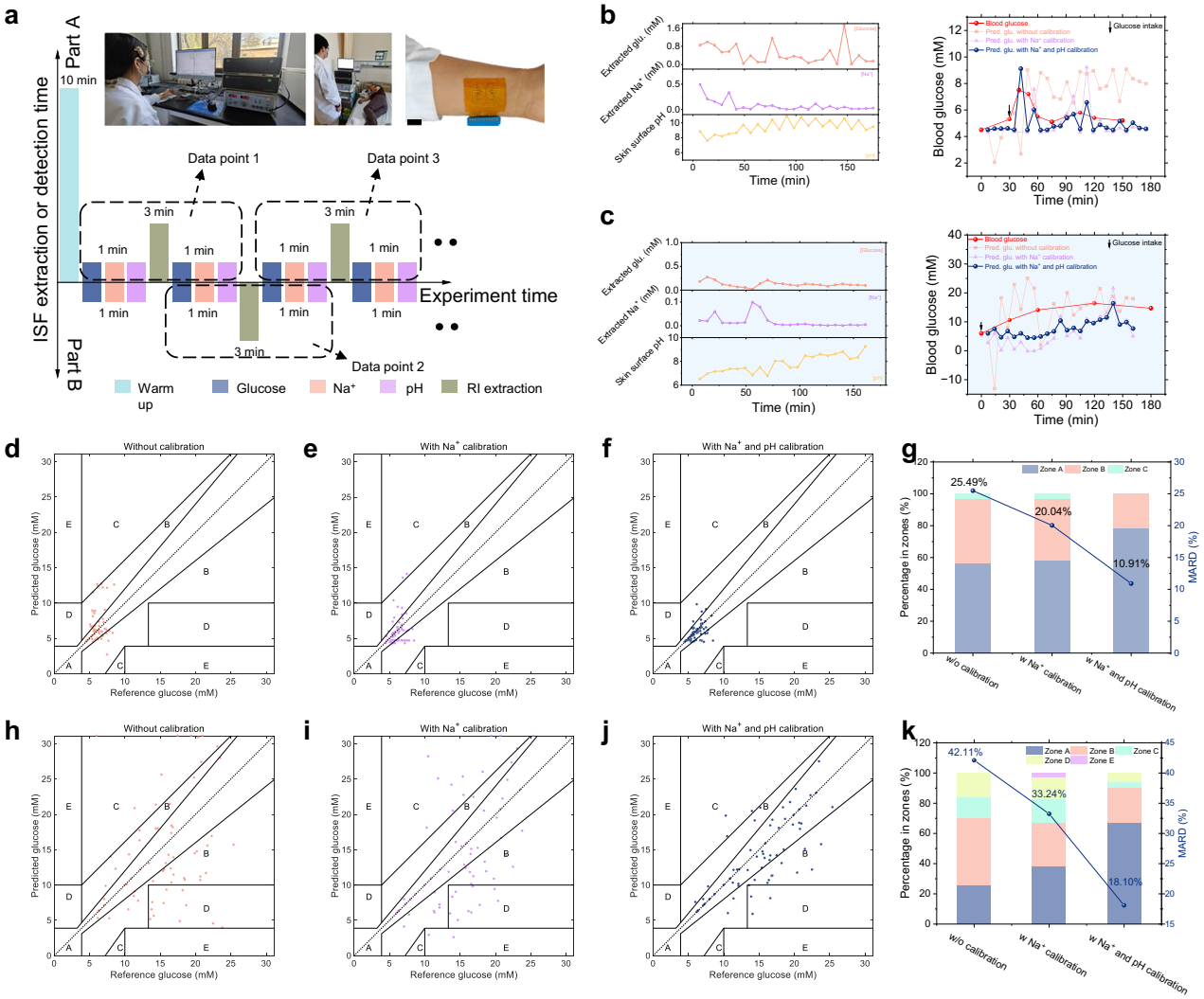

Fig. 5 | In-vivo evaluation of the calibration method and wearable device. **a** Schematic of the OGTT procedure, illustrating the relationship between the measurements and each data point related to blood glucose. Inset: Optical images of a female healthy participant (left), a male diabetic patient (middle) wearing the device, and the device applied to the arm during the OGTT (right). Scar bars, 1 cm. OGTT, oral glucose tolerance test. Results of OGTT for one healthy participant (**b**) and one diabetic patient (**c**). (Left): Variation of extracted glucose concentration, Na^+ concentration, and skin surface pH during OGTT; (Right): Results of blood glucose predictions from the wearable device under four conditions: without calibration, with Na^+ calibration, and with cooperative Na^+ and pH calibration. **d**–**f** Clarke's error grid analysis of predicted glucose concentrations versus reference glucose concentrations without calibration (**d**), with Na^+ calibration (**e**), and with cooperative Na^+ and pH calibration (**f**) for 6 healthy participants ($n = 60$ data points). **h**–**j** Clarke's error grid analysis of predicted glucose concentrations versus reference glucose concentrations without calibration (**h**), with Na^+ calibration (**i**), and with cooperative Na^+ and pH calibration (**j**) for 15 diabetic patients ($n = 70$ data points). **g**, **k** Clarke's error grid analysis of the OGTT, including percentage distribution across different zones and MARD for 6 healthy participants (**g**) and 15 diabetic patients (**k**). MARD, mean absolute relative difference.

the glucose sensor, the glucose extraction flux, and the subdermal glucose prediction capabilities. We elucidate that skin surface pH variations affect ISF extraction by altering the ZP of keratin, demonstrating a negative correlation. We also developed an epidermal electronic device to validate our hypothesis and the detailed effect. Experimental results indicate that the skin surface pH affects the electroosmosis (glucose flux) significantly while affecting the electromigration (Na^+ flux) slightly. The effect is linearity, and the electroosmotic glucose velocity increases by ~33% per skin surface pH. A pH calibration method was developed and evaluated through both in-vitro and in-vivo glucose monitoring experiments, accordingly. Significant improvements in glucose prediction accuracy were achieved, showing that the MAPE was reduced from 11.2% to 2.9% in-vitro, and the MARD was decreased from 34.44% to 14.78% in-vivo for all the volunteers, including healthy and diabetic ones. These findings underscore the pivotal role of managing pH variability in RI-based ISF extraction and accurate glucose prediction.

Nevertheless, some limitations remain. The mechanisms underlying the observed transient elevation of epidermal microfluidic pH during prolonged RI remain incompletely understood. Potential contributors include the rapid accumulation of H^+ due to their high mobility, the release of H^+ from biochemical reactions at the epidermal interface, and other, as-yet unidentified factors. These processes are complex and currently lack consensus in the literature, precluding a detailed mechanistic account at this stage and highlighting the need for further investigation. Additionally, the consequences of such transiently elevated pH on the local skin microenvironment, including potential irritation, need further systematic study.

Future work should focus on enhancing the personalization, generalizability, and safety of the pH-calibrated RI sensing platform.

More refined models of blood-to-ISF biomarkers kinetics may be developed to address physiological delays and achieve personalized calibration. In-vivo results demonstrate accurate glucose prediction within the physiological range of 4–30 mM across healthy and diabetic subjects. Future work should validate this capability by extending the tested range. Additionally, our pH-calibrated RI device can be broadly applicable to a wide range of biomarkers, including other electro-osmotically extractable analytes such as alcohol, ascorbic acid, caffeine, urea, and cortisol, which are also subject to extraction fluctuations influenced by pH. Therefore, the pH-calibrated RI model and device can be extended to other extractable biomarkers, enabling precise ISF-based multi-biomarker detection. To ensure safety in long-term applications, future device iterations may explore methods to protect the skin under extreme pH conditions and incorporate circuit protection features such as real-time impedance monitoring, enabling automatic power cut-off in response to abnormal current or impedance changes.

Methods

Materials

Glucose, sodium chloride (NaCl), potassium chloride (KCl), calcium chloride ($CaCl_2$), ascorbic acid (AA), uric acid (UA), dopamine (DA), Nafion solution, polyimide (PI) film, keratin azure (K8500), glucose oxidase (GOx), polyvinyl butyral (PVB), poly(3,4-ethylenedioxythiophene)-polystyrene sulfonate (PEDOT:PSS), and platinum nanoparticles (PtNPs) were purchased from Sigma-Aldrich (Shanghai, China). Chitosan (CS), poly(vinyl chloride) (PVC), industrial-grade multi-walled carbon nanotubes (MWCNTs), glacial acetic acid, glycerol, Na^+ carrier X, sodium tetrakis[3,5-bis(trifluoromethyl)phenyl] borate (Na-TFPB), dioctyl sebacate (DOS), Hydrogen Ionophore I (Tridodecylamine), potassium tetraphenylborate (KTClPB), cyclodextrin (CYC), Polyvinyl butyral (PVB), Pluronic F-127, and carbinol were prepared by HEOWNS (Tianjin, China). Deionized water (DI), phosphate-buffered saline (PBS, pH 7.2–7.4), and tris(hydroxymethyl) aminomethane (Tris)-HCl buffer were prepared by Huaying Prosperous Technology Co., Ltd. (Tianjin, China). All reagents were of analytical grade and used without further purification. Polyimide (PI) film was purchased from Leviathan Technology Co., Ltd (Tianjin, China). Ag/AgCl ink was supplied by Sun Chemical Co., Ltd. (UK). Prussian blue-doped carbon (PBC) ink and Ag conductive ink were provided by Gaintzor Electronic Technology Co., Ltd. (Qingdao, China). Medical adhesive tape (3M-2477P) was acquired from 3 M Medical Materials & Technologies (USA). Connectors (65801-008LF) were purchased from Amphenol (USA). Franz diffusion cells were purchased from Shanghai Chemical Laboratory Equipment Co., Ltd. (Shanghai, China). Strat-M® membranes (47 mm disks, 300 µm thickness) for transdermal ISF extraction were obtained from EMD Millipore Corporation (Billerica, USA). The TPY-2 transdermal diffusion apparatus was purchased from Huanghai Pharmaceutical Testing Instruments Co., Ltd. (Shanghai, China) for precise temperature control and magnetic stirring of the ISF. A constant current source (ZF-9, Shanghai Zhengfang Electronic & Electrical Co., Ltd.) was used to provide a 150 µA cm^{-2} current density for RI extraction. All electrochemical characterizations were performed with an electrochemical workstation (CHI 660E, Shanghai Chenhua Instrument Co., Ltd.).

Fabrication and preparation of the wearable device

Screen printing process. The fabrication process of the device is depicted in Supplementary Fig. 4. Firstly, the surface of the PI film (50 µm thickness) was cleaned using an alcohol wipe to remove surface contaminants. After cleaning, the PI substrate was subjected to O_2 plasma treatment (TS-PL10MA, Shenzhen Tonson Tech Automation Equipment Co., Ltd.) to eliminate organic impurities and enhance the surface's hydrophilicity. This treatment was carried out under radio frequency power of 300 W, with a flow rate of 100 mL min^{-1} for 90 s. The treatment resulted in improved surface hydrophilicity (Supplementary Fig. 2), which is critical for subsequent electrode printing and functional modification. Electrodes were printed on the treated PI substrate using a screen-printing method (420 mesh screen, HP-AL series, Shanghai Xuanting Screen Printing Equipment Co., Ltd.), which was performed in a layer-by-layer process. The initial step was printing an Ag conducting layer on the PI substrate, which was essential for ensuring good electrical conductivity. Then an Ag/AgCl layer was deposited on the Ag conducting layer, serving as the ISF extraction electrode and, importantly, the reference electrode (RE) for the glucose, Na^+, and pH sensors. Finally, a PBC layer was added to function as the working electrode (WE) for the glucose, Na^+, and pH sensors, thus completing the construction of this screen-printed electrodes fabrication. Each printed layer was cured at 120 °C for 3 min to ensure adequate adhesion and functionality. Non-sensing areas were encapsulated using a waterproof, skin-adhering, double-sided acrylic medical adhesive tape (3M-2477P, USA). The patterned structure of the sensor was realized by employing laser engraving technology using the Universal VLS2.30 Laser System (USA). The operation parameters were set as follows: a power level of 80%, a speed of 30%, and the laser engraving process was repeated three times to enable subsequent Functional modification.

GOx membrane solution preparation. GOx lyophilized powder (10 KU, Sigma) was dissolved in 555 µL of PBS to prepare a GOx solution with a concentration of approximately 100 mg mL^{-1}. This solution was then diluted to obtain a final concentration of 10 mg mL^{-1}. To prepare the chitosan precursor solution for embedding GOx, 10 mL of DI was added to 0.1 g of chitosan (1 wt%), followed by the addition of 30 µL of glacial acetic acid (0.3 v/v%) and 1 mL of glycerol (10 v/v%). The mixture was heated at 80 °C and stirred for 2 h. Subsequently, 0.1 mL of PtNPs aqueous solution was incorporated to complete the chitosan precursor solution. The prepared GOx solution (10 mg mL^{-1}) was mixed with the chitosan precursor solution in a 2:1 volume ratio to yield the GOx membrane solution, which was stored at 4 °C for future utilization.

Na^+ and H^+ selective membrane solution preparation. The Na^+ selective membrane solution was prepared by dissolving 2 mg of Na^+ carrier X (97%), 1 mg of Na-TFPB (97%), and 131 mg of DOS in 708 µL of CYC, ensuring complete dissolution. Afterward, 66 mg of PVC was added and ultrasonicated for 30 min to achieve a homogeneous solution, forming the Na^+ selective membrane solution. For the pH sensor selective membrane, the Na^+ carrier was replaced with Tridodecylamine and the Na-TFPB was replaced with KTClPB, while the other steps and ratios remained unchanged.

Preparation of reference membrane solution for Na^+ and pH sensors. The reference membrane solution for both the Na^+ and pH sensors was prepared by dissolving 0.2 mg of MWCNTs, 2 mg of pluronic F-127, 79.1 mg of PVB, and 50 mg of NaCl in 1 mL of anhydrous methanol. MWCNTs, F127, and NaCl were first dissolved in methanol to form a uniform solution, with NaCl reaching saturation. Following this, PVB was added to the mixture and ultrasonicated for 20 min to ensure complete dissolution of PVB. The final reference membrane solution was stored at 4 °C to ensure adequate stabilization prior to use.

Modification process of the functional layer. A 1 µL aliquot of the GOx membrane solution was individually applied to the WE on both Part A and Part B of the glucose sensors. The solution was left to naturally solidify at room temperature for 30 min. Subsequently, a 1 µL aliquot of PEDOT:PSS aqueous solution was separately applied to the WE on both Part A and Part B of the Na^+ and pH sensors. The solution was allowed to solidify at room temperature for 1 h, thereby forming a conductive polymer layer. A 1 µL aliquot of Na^+ selective membrane

solution was subsequently applied to the WE of the Na^+ sensors, while a 1 µL aliquot of H^+ selective membrane solution was applied to the WE of the pH sensors, both on Part A and Part B of the device. The electrodes were then allowed to dry at room temperature for 4 h. Finally, a 30 µL aliquot of Nafion (5 wt%, Sigma) was diluted with alcohol to a 1 wt % concentration and applied to both part A and part B of the prepared device. After curing at room temperature for 1 h, the device was fully prepared and stored at 4 °C for preservation. Structurally, each part comprises a semi-circular Ag/AgCl electrode for RI extraction, a glucose sensor with a PBC WE and a quarter-circular Ag/AgCl RE, a circular PBC WE for the Na^+ sensor, a circular PBC WE for the pH sensor, and a shared quarter-circular Ag/AgCl RE for both the Na^+ and pH sensors. The detailed structure of the electrode is shown in Supplementary Fig. 3.

Activation process of the device. To ensure stable potential measurements of the ion sensor and eliminate errors caused by baseline drift, the Na^+ and pH sensors were immersed for 2 h in a Tris-HCl buffer solution at pH 7 containing 0.1 mM NaCl for activation prior to in vivo testing.

Characterization of the wearable device

Electrochemical characterization of the glucose sensor. All electrochemical tests were conducted using the CHI 660E electrochemical workstation. Cyclic voltammetry (CV) scans were performed within the voltage range of −0.6 V to +0.6 V in 1× PBS (0.01 M, pH = 7.2–7.4), with a scan rate of 0.1 V s^{-1}. H_2O_2, an intermediate product of glucose oxidation, was first measured to assess the performance of PBC WE. Typically, the WE requires CV scans to remove surface impurities and identify the optimal bias voltage, which was found to be −0.1 V (Supplementary Fig. 8a, b). CV scans at different scan rates showed a linear relationship between peak current and the square root of the scan rate, confirming that the H_2O_2 reaction is diffusion-controlled (Supplementary Fig. 8c, d). For H_2O_2 and glucose testing, the i-t curves were carried out for 60 s, with the steady-state current recorded at the 60-s mark. Stepwise testing revealed a good linear response between sensor current and H_2O_2 concentration (Supplementary Fig. 8e), with linear sensitivity of 441 nA mM^{-1} observed ranging the 0–5 mM (Supplementary Fig. 8f). The glucose sensor testing follows a similar procedure as H_2O_2, with an initial CV scan determining the optimal bias voltage of −0.1 V (Supplementary Fig. 9a, b). CV results at different scan rates also showed a linear correlation between peak current and the square root of the scan rate, confirming that the glucose reaction is diffusion-controlled (Supplementary Fig. 9c). Therefore, the current can be linearly fitted to concentration using the Cottrell equation. The sensitivity of glucose within the range of 3–30 mM is 28.22 nA mM^{-1} (Supplementary Fig. 9d). The selectivity of the glucose sensor was assessed by immersing the glucose sensor into a 10 mL Tris-HCl solution at pH 7.4 (Fig. 2g, Supplementary Fig. 9e, f, g). Starting at 100 s, glucose (0.5/5 mM), NaCl (14/140 mM), KCl (0.4/4 mM), $CaCl_2$ (0.25/2.5 mM), uric acid (0.01/0.1 mM), dopamine (0.01/0.1 mM), ascorbic acid (0.01/0.1 mM), fructose (0.1/1 mM) and glucose (1/10 mM) were sequentially added every 60 s. The solution was stirred continuously for 1 min to facilitate stability before each detection.

The enzyme activity of GOx was evaluated by measuring the concentration of H_2O_2 generated by GOx-catalyzed glucose at different pH values. The reaction mixture consisted of glucose oxidase (10 mg mL^{-1}) and glucose solutions (10 mM) in a 1:1 v/v ratio (prepared in Tris-HCl buffer), incubated for 1 h before measurement The UV ABS test was based on the Trinder's reaction for H_2O_2, where a standard curve for H_2O_2 concentration was obtained by measuring UV ABS at 500 nm (Supplementary Fig. 10a). A solution of 0.2 mM phenol and 0.2 mM 4-AAP in PBS buffer, along with 0.25 mg mL^{-1} HRP solution, were prepared for testing. Different concentrations of H_2O_2 (10 mM, 20 mM, 30 mM, 40 mM, 50 mM) were added to the reaction mixture, followed by 500 µL of HRP solution. The mixture was shaken for 5 min at 200 rpm using a shaking incubator (SK-L180-S, DLAB). The reaction solution was transferred to a microplate for analysis using an enzyme-linked immunosorbent assay reader (Feyond-300, Hangzhou Aosheng Instrument Co., Ltd). The UV ABS at 500 nm for different H_2O_2 concentrations was plotted to obtain the standard curve (Supplementary Fig. 10b, c). The fitting results of the ABS of H_2O_2 and pH value also show a quadratic function curve, which is similar to the relationship between glucose sensitivity and pH, demonstrating its effectiveness (Supplementary Fig. 10d).

Electrochemical characterization of the Na^+ and pH sensors. The Na^+ and pH sensors, based on open circuit potential (OCP), were measured over a duration of 60 s, with the steady-state voltage taken at the 60-s mark. The selectivity of the Na^+ sensor was evaluated by immersing the Na^+ sensor into a 10 mL Tris-HCl solution at pH 7.4 (Fig. 2o, Supplementary Fig. 12c). Starting at 100 s, various substances were sequentially added every 60 s, including NaCl (50 mM), KCl (4 mM), $CaCl_2$ (2.5 mM), uric acid (0.1 mM), dopamine (0.1 mM), ascorbic acid (0.1 mM), glucose (5 mM), fructose (1 mM) and NaCl (200 mM) were sequentially added every 60 s. The selectivity of the pH sensor was assessed by immersing the pH sensor into a 10 mL Tris-HCl solution at pH 6.6 (Fig. 2s, Supplementary Fig. 13d). Starting at 100 s, NaCl (140 mM), KCl (4 mM), $CaCl_2$ (2.5 mM), uric acid (0.1 mM), dopamine (0.1 mM), ascorbic acid (0.1 mM), glucose (5 mM), fructose (1 mM) and Tris-HCl buffer (pH 7.6) were sequentially added every 60 s. Prior to each test, the solution was continuously for 1 min to facilitate the stability of all substances added to the reaction system.

Mechanical evaluation of the wearable device. The fabricated wearable device was evaluated using an environment-controlled flexible electronic testing system (FE-SDT, SINOAGG, Beijing). This testing included measurements of the resistance of the RI electrodes before and after bending, as well as electrochemical performance tests of the sensors under different bending conditions. The bending test consisted of two phases: the bending process and the recovery process, which together formed a complete cycle. The bending limit was set to 50% of the sensor's flexibility (approximately 90°), with a waiting time of 10 s once the limit was reached. The resistance testing during the bending process was conducted over two cycles (Supplementary Fig. 14). To evaluate the stability of electrochemical performance, the device was tested for the steady-state current of glucose, the steady-state voltage of Na^+, and the steady-state voltage of pH after undergoing different numbers of bending cycles (0, 10, 30, 50, and 100 bends) (Supplementary Fig. 15). These tests allowed for a comprehensive assessment of the sensor's mechanical performance and its ability to maintain stability under wearable applications.

Experimental validation of effect of skin surface pH on RI

Given the challenges presented by uncontrollable factors, including human skin temperature, skin impedance, and ISF flow rate, experiments were employed to exclusively evaluate the impact of skin surface pH on RI. The ISF extraction and testing system was constructed using Strat-M® transdermal membranes (47 mm in diameter, 300 µm in thickness) to simulate human skin. A Franz diffusion cell setup was employed, with the donor and receiver compartments designed to mimic the ISF extraction process. The receiver chamber contained 3 mL of Tris-HCl buffer solution at varying pH levels (ranging from pH 5 to 10). Commercial Ag/AgCl electrodes were used as the RI electrodes to minimize ISF extraction fluctuations related to electrode degradation during RI. A constant current source was applied, delivering a 0.5 mA current for 15 min to facilitate the ISF extraction (Supplementary Fig. 16). Firstly, we assessed the effect of varying skin surface pH on Na^+ extraction flux. The donor chamber in the Franz cell contained 15 mL of Tris-HCl buffer solution with 140 mM NaCl and either 15 mM

or 30 mM glucose at pH 7.4. Then we investigated the influence of skin surface pH on glucose extraction flux. This experimental setup provided a controlled environment to evaluate the pH-dependent changes in RI.

Preparation of the in-vitro ISF extraction and testing system

Due to the interference of uncontrollable factors such as skin temperature, skin impedance, and interstitial fluid flow rate, the effect of pH as a single variable on glucose extraction flux was investigated through in vitro simulation experiments. Figure 4a, Supplementary Fig. 24 illustrates the setup of the system, which includes a constant current source to supply the RI extraction current, a TPY-2 intelligent transdermal diffusion instrument to maintain a constant temperature of 37 ± 0.1 °C, and a magnetic stirrer to simulate ISF flow. The Strat-M® transdermal membrane (47 mm diameter, 300 µm thickness) mimics human skin, while two electrochemical workstations (CHI660E) are used to measure glucose concentration, Na^+ concentration, and pH on the membrane surface. A switch controls the ISF extraction and detection process automatically, and a computer is used for data acquisition and processing. RI is set as 150 µA cm^{-2} for 3 min for one extraction cycle, which is selected for subsequent glucose extraction testing.

To reduce fluctuations in ISF extraction induced by electrode degradation, alternating current polarity was utilized between consecutive extractions (Supplementary Figs. 25, 26). This approach helped maintain the performance of RI electrodes and ensured more stable extraction conditions. To further minimize potential errors from repeated ISF extractions, glucose and pH measurements from five consecutive cycles were selected for validation, providing a more reliable dataset for assessing extraction consistency and the accuracy of glucose predictions.

OGTT Procedure

The OGTT data collection process is illustrated in Fig. 5a. After attaching the prepared device to the skin, a 10-min warm-up was initially conducted to ensure tight adhesion of the device to the skin and stabilizes the RI current. Following this, glucose, Na^+, and pH are sequentially measured in both parts of the device; subsequent measurements follow the same protocol. After the initial measurements, ISF is extracted for 3 min, with the extraction direction set from Part B to Part A. Measurements are then repeated, with the first set of valid data labeled as Data point 1. The polarity is then switched to obtain subsequent data points, such as Data point 2, Data point 3, and so on. The time lag between blood glucose and ISF glucose is established as 10 min, consistent with commonly reported physiological lags[62,63] (Supplementary Table 8).

After an 8–14 h fasting period, 6 healthy volunteers and 15 diabetic patients participated in a 3-h OGTT. Participants consumed a 250 mL bottle of glucose solution containing 75 g glucose over a 5-min period. Blood glucose levels were measured using a commercial glucometer (ACCU-CHEK, Switzerland) for healthy volunteers and venous blood sampling points for diabetic patients as the reference. The experimental setup included the fabricated epidermal device, a constant current source, electrochemical workstations, a switch circuit, and a laptop. A wearable device was applied to the participants' forearm for continuous glucose, Na^+, and pH detection, with RI performed at a current density of 150 µA cm^{-2} for 3 min for one extraction cycle. After each extraction cycle, glucose, Na^+, and pH levels were measured for one minute. The polarity of the RI current was alternated between successive cycles to reduce the consumption of RI electrodes. The performance of the proposed skin surface pH calibration method was evaluated by comparing the predicted blood glucose levels with reference measurements using Clarke's error grid analysis.

Ethics

Every participant provided written informed consent prior to the study procedure. The in-vivo experiments were approved by the Ethical Committee of Tianjin University, China; the identification number (ID) of the certification is TJVE-2024-161. The ethical review for the experiments of diabetic volunteers has been officially approved by the Ethical Committee of Tianjin Medical University Chu Hsien-I Memorial Hospital & Institute of Endocrinology, China; the identification number (ID) of the certification is ZXYJNYYKMEC2023-39.

Reporting summary

Further information on research design is available in the Nature Portfolio Reporting Summary linked to this article.

Data availability

All data supporting the findings of this study are available within the article and its supplementary files. Any additional requests for information can be directed to and will be fulfilled by the corresponding authors. Source data are provided with this paper.

Code availability

The codes used for simulation and data measurement are available from the corresponding author with upon reasonable request.

References

1. Kim, J., Campbell, A. S., de Ávila, B. E.-F. & Wang, J. Wearable biosensors for healthcare monitoring. *Nat. Biotechnol.* **37**, 389–406 (2019).
2. Chen, S. et al. Wearable flexible microfluidic sensing technologies. *Nat. Rev. Bioeng.* **1**, 950–971 (2023).
3. Mahato, K. et al. Hybrid multimodal wearable sensors for comprehensive health monitoring. *Nat. Electron.* **7**, 735–750 (2024).
4. Zhong, D. et al. High-speed and large-scale intrinsically stretchable integrated circuits. *Nature* **627**, 313–320 (2024).
5. Zhang, B. et al. A three-dimensional liquid diode for soft, integrated permeable electronics. *Nature* **628**, 84–92 (2024).
6. Brasier, N. et al. Applied body-fluid analysis by wearable devices. *Nature* **636**, 57–68 (2024).
7. Xu, Y. et al. In-ear integrated sensor array for the continuous monitoring of brain activity and of lactate in sweat. *Nat. Biomed. Eng.* **7**, 1307–1320 (2023).
8. Wang, M. et al. A wearable electrochemical biosensor for the monitoring of metabolites and nutrients. *Nat. Biomed. Eng.* **6**, 1225–1235 (2022).
9. Sempionatto, J. R. et al. An epidermal patch for the simultaneous monitoring of haemodynamic and metabolic biomarkers. *Nat. Biomed. Eng.* **5**, 737–748 (2021).
10. Ye, C. et al. A wearable aptamer nanobiosensor for non-invasive female hormone monitoring. *Nat. Nanotechnol.* **19**, 330–337 (2024).
11. Meng, X., Li, Z., Yue, W., Zhang, L. & Xie, Z. Toward at-home and wearable monitoring of female hormones: emerging nanotechnologies and clinical prospects. ACS Sens. **10**, 54–75 (2025).
12. Arwani, R. T. et al. Stretchable ionic–electronic bilayer hydrogel electronics enable in situ detection of solid-state epidermal biomarkers. *Nat. Mater.* **23**, 1115–1122 (2024).
13. Zargartalebi, H. et al. Active-reset protein sensors enable continuous in vivo monitoring of inflammation. *Science* **386**, 1146–1153 (2024).
14. Tu, J. et al. A wireless patch for the monitoring of C-reactive protein in sweat. *Nat. Biomed. Eng.* **7**, 1293–1306 (2023).
15. Sempionatto, J. R., Lasalde-Ramírez, J. A., Mahato, K., Wang, J. & Gao, W. Wearable chemical sensors for biomarker discovery in the omics era. *Nat. Rev. Chem.* **6**, 899–915 (2022).
16. Min, J. et al. Skin-interfaced wearable sweat sensors for precision medicine. *Chem. Rev.* **123**, 5049–5138 (2023).

17. Gao, W. et al. Fully integrated wearable sensor arrays for multiplexed in situ perspiration analysis. *Nature* **529**, 509–514 (2016).
18. Xu, C. et al. A physicochemical-sensing electronic skin for stress response monitoring. *Nat. Electron.* **7**, 168–179 (2024).
19. Zhong, B. et al. Interindividual- and blood-correlated sweat phenylalanine multimodal analytical biochips for tracking exercise metabolism. *Nat. Commun.* **15**, 624 (2024).
20. Nyein, H. Y. Y. et al. A wearable patch for continuous analysis of thermoregulatory sweat at rest. *Nat. Commun.* **12**, 1823 (2021).
21. Keum, D. H. et al. Wireless smart contact lens for diabetic diagnosis and therapy. *Sci. Adv.* **6**, eaba3252 (2020).
22. Arakawa, T. et al. A wearable cellulose acetate-coated mouthguard biosensor for in vivo salivary glucose measurement. *Anal. Chem.* **92**, 12201–12207 (2020).
23. Zhang, J. et al. A wearable self-powered biosensor system integrated with diaper for detecting the urine glucose of diabetic patients. *Sens. Actuators B: Chem.* **341**, 130046 (2021).
24. Chen, Y. et al. Skin-like biosensor system via electrochemical channels for noninvasive blood glucose monitoring. *Sci. Adv.* **3**, e1701629 (2017).
25. De la Paz, E. et al. Extended noninvasive glucose monitoring in the interstitial fluid using an epidermal biosensing patch. *Anal. Chem.* **93**, 12767–12775 (2021).
26. Yin, S. et al. A long lifetime and highly sensitive wearable microneedle sensor for the continuous real-time monitoring of glucose in interstitial fluid. *Biosens. Bioelectron.* **244**, 115822 (2024).
27. Jin, X. et al. Fully integrated flexible biosensor for wearable continuous glucose monitoring. *Biosens. Bioelectron.* **196**, 113760 (2022).
28. Friedel, M. et al. Opportunities and challenges in the diagnostic utility of dermal interstitial fluid. *Nat. Biomed. Eng.* **7**, 1541–1555 (2023).
29. Samant, P. P. et al. Sampling interstitial fluid from human skin using a microneedle patch. *Sci. Transl. Med.* **12**, eaaw0285 (2020).
30. Hanna, J. et al. Noninvasive, wearable, and tunable electromagnetic multisensing system for continuous glucose monitoring, mimicking vasculature anatomy. *Sci. Adv.* **6**, eaba5320 (2020).
31. Lin, T., Mayzel, Y. & Bahartan, K. The accuracy of a non-invasive glucose monitoring device does not depend on the clinical characteristics of people with type 2 diabetes mellitus. *J. Drug Assess.* **7**, 1–7 (2018).
32. Yang, D. et al. Glucose sensing using surface-enhanced raman-mode constraining. *Anal. Chem.* **90**, 14269–14278 (2018).
33. Cho, O. K., Kim, Y. O., Mitsumaki, H. & Kuwa, K. Noninvasive measurement of glucose by metabolic heat conformation method. *Clin. Chem.* **50**, 1894–1898 (2004).
34. Zhu, W. et al. Effect of interstitial fluid pH on transdermal glucose extraction by reverse iontophoresis. *Biosens. Bioelectron.* **235**, 115406 (2023).
35. Tianyi, S., Yulong, Z., Yanzhen, J., Chen, C.-J. & Liu, J.-T. Micro interstitial fluid extraction and detection device integrated with the optimal extraction conditions for noninvasive glucose monitoring. *Biosens. Bioelectron.* **237**, 115515 (2023).
36. Chang, T. et al. Highly integrated watch for noninvasive, continual glucose monitoring. *Microsyst. Nanoeng.* **8**, 25 (2022).
37. Kusama, S. et al. Transdermal electroosmotic flow generated by a porous microneedle array patch. *Nat. Commun.* **12**, 658 (2021).
38. Pu, Z. et al. A thermal activated and differential self-calibrated flexible epidermal biomicrofluidic device for wearable accurate blood glucose monitoring. *Sci. Adv.* **7**, eabd0199 (2021).
39. Glikfeld, P., Hinz, R. S. & Guy, R. H. Noninvasive sampling of biological fluids by iontophoresis. *Pharm. Res.* **6**, 988–990 (1989).
40. Tierney, M. J., Tamada, J. A., Potts, R. O., Jovanovic, L. & Garg, S. Clinical evaluation of the GlucoWatch® biographer: a continual, non-invasive glucose monitor for patients with diabetes. *Biosens. Bioelectron.* **16**, 621–629 (2001).
41. Zheng, H. et al. Reverse iontophoresis with the development of flexible electronics: a review. *Biosens. Bioelectron.* **223**, 115036 (2023).
42. Li, C. et al. A flexible glucose biosensor modified by reduced-swelling and conductive zwitterionic hydrogel enzyme membrane. *Anal. Bioanal. Chem.* **416**, 4849–4860 (2024).
43. Flavin, M. T. et al. Bioelastic state recovery for haptic sensory substitution. *Nature* **635**, 345–352 (2024).
44. Fu, X., Cheng, W., Wan, G., Yang, Z. & Tee, B. C. K. Toward an AI era: advances in electronic skins. *Chem. Rev.* **124**, 9899–9948 (2024).
45. Yoon, H. & Dagdeviren, C. Towards device technologies non-invasive to our daily lives. *Nat. Commun.* **16**, 1027 (2025).
46. Liu, J. et al. Bioresorbable shape-adaptive structures for ultrasonic monitoring of deep-tissue homeostasis. *Science* **383**, 1096–1103 (2024).
47. Heng, W. et al. A smart mask for exhaled breath condensate harvesting and analysis. *Science* **385**, 954–961 (2024).
48. Wang, W. et al. Neuromorphic sensorimotor loop embodied by monolithically integrated, low-voltage, soft e-skin. *Science* **380**, 735–742 (2023).
49. Shi, J. et al. Active biointegrated living electronics for managing inflammation. *Science* **384**, 1023–1030 (2024).
50. Lipani, L. et al. Non-invasive, transdermal, path-selective and specific glucose monitoring via a graphene-based platform. *Nat. Nanotechnol.* **13**, 504–511 (2018).
51. Giri, T. K., Chakrabarty, S. & Ghosh, B. Transdermal reverse iontophoresis: A novel technique for therapeutic drug monitoring. *J. Control. Release* **246**, 30–38 (2017).
52. Curdy, C., Kalia, Y. N. & Guy, R. H. Post-iontophoresis recovery of human skin impedance in vivo. *Eur. J. Pharm. Biopharm.* **53**, 15–21 (2002).
53. Manda, P., Angamuthu, M., Hiremath, S. R., Raman, V. & Murthy, S. N. Iontophoretic drug delivery for the treatment of scars. *J. Pharm. Sci.* **103**, 1638–1642 (2014).
54. Abe, Y. & Nishizawa, M. Electrical aspects of skin as a pathway to engineering skin devices. APL Bioeng. 5, 041509 (2021).
55. Dukhin A. S., Xu R. Chapter 3.2.5 - Zeta-potential measurements. In: *Characterization of Nanoparticles* (eds Hodoroaba V.-D., Unger W. E. S., Shard A. G.). Elsevier (2020).
56. Smorodin, V. Y. Concerning a percolation concept of zeta potential and electrokinetic phenomena in bio-systems. *Biophys. J.* **98**, 79a (2010).
57. De Luca, C. & Valacchi, G. Surface lipids as multifunctional mediators of skin responses to environmental stimuli. *Mediators Inflamm.* **2010**, 321494 (2010).
58. Fukuda, K. et al. Three stepwise pH progressions in the stratum corneum for homeostatic maintenance of the skin. *Nat. Commun.* **15**, 4062 (2024).
59. Santi, P. & Guy, R. H. Reverse iontophoresis—Parameters determining electroosmotic flow: I. pH and ionic strength. *J. Control. Release* **38**, 159–165 (1996).
60. Kalia, Y. N., Naik, A., Garrison, J. & Guy, R. H. Iontophoretic drug delivery. *Adv. Drug Deliv. Rev.* **56**, 619–658 (2004).
61. Sieg, A., Guy, R. H. & Delgado-Charro, M. B. Reverse iontophoresis for noninvasive glucose monitoring: the internal standard concept. *J. Pharm. Sci.* **92**, 2295–2302 (2003).
62. Rebrin, K., Sheppard, N. F. & Steil, G. M. Use of subcutaneous interstitial fluid glucose to estimate blood glucose: revisiting delay and sensor offset. *J. Diabetes Sci. Technol.* **4**, 1087–1098 (2010).
63. Barry Keenan, D., Mastrototaro, J. J., Weinzimer, S. A. & Steil, G. M. Interstitial fluid glucose time-lag correction for real-time continuous glucose monitoring. *Biomed. Signal Process. Control* **8**, 81–89 (2013).

Acknowledgments
This work was supported by the National Key R&D Program of China (No. 2022YFB3203700 (Z.P.)), National Natural Science Foundation of China (No. 82072012 (D.L.) and No. 82102230 (Z.P.)), and Young Scientific and Technological Talents in Tianjin (No. QN20230347 (Z.P.)).

Author contributions
Z.P., H.Y. and W.Z. conceived the study. Z.P., H.Y. and W.Z. contributed to the methodology. W.Z., X.L., M.W., J.H., Y.L., C.J., Y.M., Z.Z., M.D., P.G., W.L., M.L. and Z.S. conducted the investigation. W.Z. was responsible for the visualization. Z.P. and D.L. acquired funding. Z.P. and D.L. supervised the project. Z.P. and W.Z. wrote the original draft, while Z.P., W.Z., X.Z., C.L. and H.Z. reviewed and edited the manuscript.

Competing interests
The authors declare no competing interests.

Additional information
Supplementary information The online version contains supplementary material available at https://doi.org/10.1038/s41467-025-65453-0.

Correspondence and requests for materials should be addressed to Zhihua Pu or Dachao Li.

Peer review information *Nature Communications* thanks Masoud Mehrgardi and the other anonymous reviewers for their contribution to the peer review of this work. A peer review file is available.